Study on Final Equilibrium State and Process of CO_2 Reacting with Fe–C Melt

WENHE WU, RONG ZHU, GUANGSHENG WEI, CHUNYANG WANG, and HAIJUAN WANG

To study the final equilibrium state and process of CO_2 injecting into the Fe–C melt with different initial carbon contents, a model was established based on the method of minimization of Gibbs free energy and the corresponding experiments were carried out in a high-temperature tube furnace. When CO_2 is continuously injected into the Fe–C melt at 1873 K, the final equilibrium state of the system is such that the carbon and oxygen contents in the melt are 0.1977 and 0.0115 wt pct, respectively, and the volume ratio of CO in the gas phase is 85.75 vol pct. When the initial $a_{[O]} \times a_{[C]}$ in the melt is greater than those in equilibrium with CO under 0.8575 atm, the CO_2 gas removes carbon from the melt. On the contrary, the role of CO_2 gas is to add carbon and oxygen to the melt. At the same time, the variation of carbon and oxygen with time obtained by experiments was different from the theoretical calculation at extremely low carbon content, which requires further study.

I. INTRODUCTION

As a gaseous medium, CO_2 is widely used in steelmaking processes as a replacement for $O_2/N_2/Ar$ gases. At present, it is being used for the combined top and bottom blowing in the basic oxygen furnace (BOF) and bottom blowing in the electric arc furnace (EAF). It is also adopted in the ladle furnace (LF), and as the bottom blowing and lifting gas in the Rheinstahl–Heraeus (RH). Theoretical analyses and laboratory experiments were carried out in an argon-oxygen decarburization furnace (AOD) and a vanadium-extraction converter (de-V BOF), which can reduce the amount of dust and the total Fe content (TFe) in the slag and improve the dephosphorization efficiency. At the same time, CO_2 can also improve the purity of molten steel in the LF and the stirring strength in the RH, and realize selective oxidation of chromium, vanadium, and other valuable elements with carbon. Table I gives an overview of the applications of CO_2 in steelmaking processes and the results that have been obtained from the former research.[1–14] The theoretical basis for achieving the preceding effects is that CO_2 exhibits weak oxidation, which occurs through the reaction $CO_2 + [C] = 2CO$. The reaction characteristics mainly include the endothermic effect that reduces the temperature of the fire point zone and controls the heating rate of molten steel, generating nearly twice the amount of gas to improve the stirring intensity in the furnace, and selective oxidation of carbon and other valuable elements under different pressures and liquid steel compositions. However, these studies were carried out mostly in the industrial scale and did not go deep into theoretical analysis.

Besides, many researchers have studied the decarburization kinetics of CO_2 as an oxidizing gas in liquid steel containing carbon in the laboratory.[15–36] Most studies have evaluated the influence of the composition of multicomponent gaseous mixtures, such as O_2–CO_2–Ar, gas phase flow rate and pressure, temperature, and liquid steel composition (carbon, sulfur, silicon, manganese, chromium, vanadium, *etc*.) on the decarburization kinetics and the rate-limiting steps of the decarburization reaction, as shown in Table II. As can be seen from the summary in the table, most of the research was not referring to the low and extremely low carbon Fe–C melt.

The preceding studies mainly focus on the industrial applications and decarburization kinetics of CO_2 gas used as an oxidant and stirring gas; however, the final equilibrium state of the system is not clear when CO_2 is continuously injected into the Fe–C melt, and it needs to be clarified whether CO_2 shows a decarburization effect

WENHE WU, RONG ZHU, GUANGSHENG WEI, CHUNYANG WANG, and HAIJUAN WANG are with the School of Metallurgical and Ecological Engineering, University of Science and Technology Beijing, Beijing 100083, China and also with the Research Center of Carbon Dioxide Science, University of Science and Technology Beijing, Beijing 100083, China. Contact email: wanghaijuan@ustb.edu.cn.

Table I. Application of CO₂ Gas in Steelmaking Processes

Process	Specifications	Injection Mode	Flow Rate	Liquid Steel Composition	Industrial Application Result	References
Conventional BOF	30 t	O_2–CO_2 mixed injection in top blowing	400 to 800 Nm^3/h	liquid iron	average dust generation rate reduced by 12.5 pct, whereas average T-Fe generation in dust reduced by 12.7 wt pct	1
		O_2–CO_2 mixed injection in top blowing and CO_2 injection in bottom blowing	top blowing: 500 Nm^3/h; bottom blowing: 80 to 160 Nm^3/h	liquid iron	contents of [N] and [P] in molten steel reduced by 50 and 23.33 wt pct, respectively	2
	120 t	CO_2 injection in bottom blowing	200 to 500 Nm^3/h	liquid iron	nitrogen content in finished steel reduced from 30 to 70 ppm to a level consistently lower than 40 ppm	3
	300 t	O_2–CO_2 mixed injection in top blowing	O_2–(5 to 10 vol pct) CO_2 mixed injection in top blowing	liquid iron	dephosphorization rate increased by 6.99 pct and the dust amount decreased by 2.65 pct, CO content in the furnace gas increased by 2.66 vol pct, and the converter gas volume increased by 5.24 Nm^3/t steel.	4
Dephospho-rization BOF	300 t	O_2–CO_2 mixed injection in top blowing and CO_2 injection in bottom blowing	top blowing: 2400 to 7000 Nm^3/h; bottom blowing: 800 to 3000 Nm^3/h	liquid iron	end-point carbon content increased from 3.19 to 3.26 wt pct and end-point phosphorus content decreased from 0.051 to 0.044 wt pct	5
Vanadium-Extraction BOF	laboratory research	—	—	—	top-blowing style saved more carbon during the vanadium-extraction process, whereas it oxidized more vanadium to the slag phase compared with the bottom-blowing style	6, 7
EAF	75 t	bottom blowing CO_2 gas	80 to 100 L/min	50 wt pct liquid iron and 50 wt pct scrap	average nitrogen content of the final molten steel with bottom-blown Ar is 55.6×10^{-6} whereas it is 46.2×10^{-6} with bottom-blown CO_2	8
LF	60 t/200 t	bottom blowing CO_2 gas	90 to 800 L/min	Al-killed steel	induces small additional deoxidizer losses but no deterioration in the purity of the final product.	9
	70 t	Ar–CO_2	total gas flow 20 to 300 L/min	45# grade	equal yield density of inclusions decreases where there is only a slight increase in [O] and [N] contents in molten steel under CO_2 blowing	10
RH	120 t	CO_2	80 to 100 Nm^3/h	Al-killed steel	selective oxidation of carbon and oxygen can occur between CO_2 and molten steel in vacuum; CO_2 can react with a small portion of [C], enhancing the RH stirring intensity	11–13
AOD	laboratory research	—	—	—	CO_2 injection is beneficial for reducing Cr loss in molten steel, and the reaction rate of CO_2 and C is slow; high proportion of CO_2 injection will not only make the bath temperature too low but will also prolong the smelting cycle	14

Table II. Decarburization Kinetics of Reaction Between CO_2 and Molten Steel

Liquid Composition	Experimental Method	Gas Phase Composition	Flow Rate and Pressure	Temperature	References
2 g Fe–4 wt pct C	levitated drop method	CO_2	100 to 1200 mL·min⁻¹	2053 K	[15]
300 g molten iron, containing Si, Cr, and Mn, w_C = 0.5 to 2 pct	crucible method, gas injection at 7 mm above molten pool	CO_2–Ar φCO_2 = 5.9 to 58.8 pct	1700 mL·min⁻¹	1873 K	[16]
4 to 7 g Fe–1 wt pct C	levitated drop method	CO_2–Ar φCO_2 = 0 to 8 pct	262 to 305 mL·min⁻¹	1803 K	[17]
400 g Fe–C w_C = 0.02 to 0.05 pct	crucible method, gas injection at 5 mm above molten pool	CO_2–Ar pCO_2/pAr = 1/1, 1/4, 1/5, 1/10, 1/20, and 1/40	1300 mL·min⁻¹	1873 K	[18]
Fe–C w_C = 0.02 to 0.05 pct	crucible method, gas injection at 5 mm above molten pool	Ar–CO–CO_2	1300 to 1600 mL·min⁻¹	1873 K	[19]
Fe–4 wt pct C–0.3 wt pct S Fe–0.1 wt pct C	a horizontal furnace a vertical furnace	CO–CO_2–H_2 φCO_2 = 2.2 to 9 pct CO–CO_2	U = 13 to 52 cm/s	1800 K	[20]
Fe–5/5.5 wt pct C Fe	high pressure levitation cell	CO–CO_2 φCO_2 = 1.1/2.15 pct	40 atm	1923 K	[21]
carbon-saturated liquid iron at sulfur concentrations between 0.01 and 1 wt pct	crucible method, gas injection at 3 mm above molten pool	CO_2–Ar φCO_2 = 0.25 to 0.5 pct	20 L/min 1 atm	1553 K and 1873 K	[22]
Fe–C–S w_C = 2.48 pct/0.92 pct w_S = 0.027 to 0.148 pct	levitation drop method	CO_2–CO φCO_2 = 0.25 to 0.5 pct	1000 mL/min	1973 K	[22, 23]
Fe–C_{sat} liquid alloys containing S, P, Sn, and Pb	crucible method, gas injection at 10 mm above molten pool	10 pct CO_2–Ar	10 L/min	1873 K	[24]
20 g carbon-saturated Fe–0.2 wt pct S	crucible method, gas injection at 10 mm above molten pool	Ar–CO_2–H_2O	4 to 16 L/min	1773 K	[25]
0.8 g Fe–C alloys containing S, P, and Cr	levitation drop method	CO_2–N_2–CO	0.002 to 0.01 m³/min	1723 K	[26]
0.8 g Fe–C–S alloys w_C = 3.4 pct	levitation drop method	O_2–CO_2–H_2O–H_2O–He φCO_2 = 10 to 16 vol pct	1 atm 0.01 m³/min	1723 K	[27]
80 to 110 g Fe–C–Si w_{Si} = 0.08 to 0.71 pct	crucible method, electric resistance furnace	CO_2 CO_2–Ar	10 mL/min	1573 K	[28]
90 g Fe–C–S alloys w_C = 3.77 to 4.60 pct, w_{Si} = 0.14 to 2.78 pct	vertical SiC electric resistance furnace, jets were inserted in the furnace	CO_2–O_2	10 to 12 mL/min	1573 K	[29]
800 g Fe–4 wt pct C or commercial type metal	induction melting, lance tip was kept at about 40 mm above the bath surface	CO_2–O_2–CO–Ar–N_2	4 to 14 L/min	1723 K	[30, 31]
6 kg high-purity electrolytic iron	vacuum induction furnace	Ar–CO_2	0.4 bar 0.1 L/min	1873 K	[32]
25 g Fe–Cr–C alloy in a horizontal furnace 1 kg Fe–Cr–C alloy in an induction furnace thermogravimetric analysis		O_2–CO_2	1670 mL/min	1873 K	[33]
0.7 g Fe–Cr–C_{sat} 10, 17, and 20 wt pct Cr	electromagnetic levitation method	30 vol pct CO_2–Ar	100, 1000, 3000, and 12,200 mL/min	1873 K	[34]

Table II. continued

Liquid Composition	Experimental Method	Gas Phase Composition	Flow Rate and Pressure	Temperature	References
Fe–C melts w_C = 1 to 4 pct	isotope tracing method crucible method, 1 to 2 cm of gas injection height	$^{13}CO_2$–$^{18}O_2$–Ar	30 to 60 mL/min	1873 K	35
Fe–C melts w_C = 0 to 2 to 8 pct	isotope tracing method crucible method, 2 cm of gas injection height	O_2–CO_2 $^{13}CO_2$–$^{18}O_2$	40150 mL/min	1873 K	36

in liquid steel under all carbon content ranges. In particular, there are no quantitative studies reporting the oxidation ability of CO_2 when injecting it into molten steels.

In this case, we have carried out the study on the continuous injection of CO_2 into Fe–C melts with different initial carbon contents to determine the effect law of CO_2 on the decarburization process of the Fe–C melt, in order to enrich the database of CO_2 injection in the steelmaking process.

II. THEORETICAL CALCULATION

To obtain a better understanding of how CO_2 reacts with the Fe–C melt of different initial carbon contents, a model for continuous injecting CO_2 will be set up and the composition change of components in the system will be simulated by the model.

A. Process Description

At steelmaking temperatures, the chemical reaction between the CO_2 gas and Fe–C melt is a three-phase (gas–slag–metal) coupling reaction. This reaction mainly includes the decomposition reaction of the CO_2 gas (Eq. [1]); equilibrium reaction of the CO, carbon, and oxygen in the melt (Eq. [2]); equilibrium reaction of O_2 with oxygen in the melt (Eq. [3]); and equilibrium reaction of iron and oxygen in the melt to generate FeO in the slag phase (Eq. [4]). The gas phase includes O_2, CO_2, and CO; the liquid phase includes C, O, and Fe; and the slag phase is FeO. During the smelting process, the gas phase continuously enters the system. After the CO_2 gas reacts with the components in the system, the gaseous reaction products escape from the slag–steel interface and a fresh stream of injected CO_2 reacts with the melt to form a new state.

$$CO_2 \rightleftharpoons CO + [O] \qquad [1]$$

$$CO \rightleftharpoons [C] + [O] \qquad [2]$$

$$O_2 \rightleftharpoons 2[O] \qquad [3]$$

$$Fe + [O] \rightleftharpoons FeO \qquad [4]$$

B. Modeling Assumptions

To simulate the reaction between the CO_2 gas and the Fe–C melt, the following assumptions were made.

(1) CO_2 gas is input step by step.
(2) At each step, the input CO_2 gas and the system reach thermodynamic equilibrium.
(3) Before the next calculation step, the gaseous components formed in the previous step are removed.
(4) The pressure of the gas phase is 1 atm.

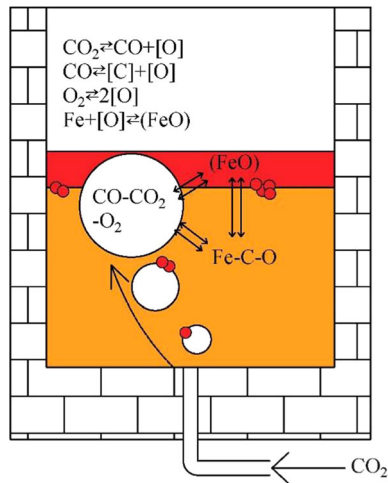Fig. 1—Schematic diagram of the reaction process between the CO_2 gas and Fe–C melt.

A schematic diagram of the reaction process between the CO_2 gas and Fe–C melt is shown in Figure 1.

C. Model Setup

A single component in the reaction system may participate in two or more reactions during the reaction process. CO gas participates in the decomposition of CO_2 gas and the equilibrium reaction of carbon and oxygen in the Fe–C melt, whereas the oxygen in the melt participates in all four of the reactions (Eqs. [1] through [4]) occurring in the system. Most of the existing research work only considers the reaction CO_2 + [C] = 2CO and fails to describe the changes in all the components of the system.

The minimum Gibbs free energy method is effective for analyzing the thermodynamic equilibrium state of multiphase coupling systems.[37–39] For any multiphase closed system, when the temperature and pressure are determined, the necessary and sufficient conditions for all reactions in the system to reach equilibrium are that the total Gibbs free energy of the closed system reaches the minimum value and the mass of each element in the system is conserved. The objective function for this problem is presented in Eq. [5].

$$
\begin{aligned}
\min \cdot G_s &= \sum_{i=1}^{C} n_i G_i = \sum_{i=1}^{C} n_i \left(G_{m,i}^{\Theta} + RT \ln a_i \right) \\
&= n_{O_2}[G_{m,O_2}^{\Theta} + RT \ln p_{O_2}] + n_{CO_2}[G_{m,CO_2}^{\Theta} \\
&\quad + RT \ln p_{CO_2}] + nCO[G_{m,CO}^{\Theta} + RT \ln p_{CO}] \\
&\quad + nC[G_{m,C}^{\Theta} + RT \ln aC] + nO[G_{m,O}^{\Theta} \\
&\quad + RT \ln aO] + nFe[G_{m,Fe}^{\Theta} + RT \ln aFe] \\
&\quad + nFeO[G_{m,FeO}^{\Theta} + RT \ln aFeO] (J)
\end{aligned}
\quad [5]
$$

where $\min \cdot G_s$ is the minimum value of G_s, J/mol; C is the total number of components in the system; $G_{m,i}^{\Theta}$ is
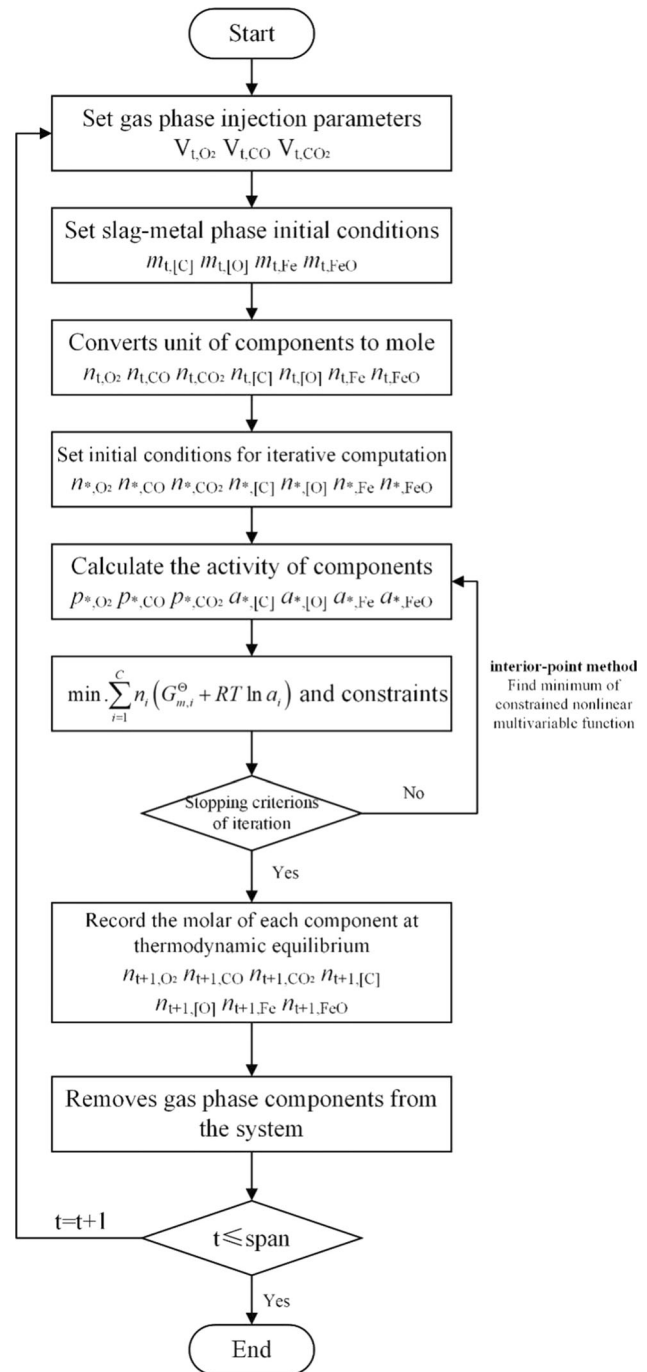

Fig. 2—Calculation flow diagram.

the standard Gibbs free energy of component i, J/mol; n_i is the mole number of component i in the system when reaching the gas–slag–metal equilibrium state, mol; p_i is the partial pressure of component i in the gas phase, atm; and a_i is the activity of component i in the melt or slag with pure material or 1 wt pct as the standard state.

The constraint conditions are given subsequently. Equations [6] through [9] represent the matter conservation of oxygen, carbon, and iron in the

Table III. Standard Molar Gibbs Free Energy and Standard State of Components in the System

Phase	Material	Standard State	Gibbs Free Energy of Standard Molar Formation $\Delta_f G_m^\theta$ J/mol	Reaction Equation	Equation Order
Gas Phase	O_2	pure substance in gas phase	0	—	—
	CO	pure substance in gas phase	$-117{,}934.9 - 84.01 \times T$	$C(graphite) + 0.5O_2 = CO$	[10]
	CO_2	pure substance in gas phase	$-396{,}476.3 - 0.045 \times T$	$C(graphite) + O_2 = CO_2$	[11]
Metal Phase	C	1 wt pct Henrian activity	$22{,}590 - 42.26 \times T$	$C(graphite) = [C]$	[12]
	O		$-117{,}150 - 2.89 \times T$	$0.5O_2 = [O]$	[13]
	Fe	pure substance in liquid phase	$13{,}762 - 7.6 \times T$	$Fe\,(s) = Fe\,(l)$	[14]
Slag Phase	FeO	pure substance in liquid phase	$-229{,}114.5 + 42.996 \times T$	$Fe\,(s) + 0.5O_2 = FeO\,(l)$	[15]

system; the molar amount of each component is non-negative.

$$\sum nO = 2 \times nO_2 + nCO + 2 \times nCO_2 + nO + nFeO \tag{6}$$

$$\sum nC = nCO + nCO_2 + nC \tag{7}$$

$$\sum nFe = nFe + nFeO \tag{8}$$

$$n_i \geq 0 \tag{9}$$

For calculating or modeling the variation of the gas–metal–slag phase during CO_2 reacting with the Fe–C melt, a flow chart will be adopted in the current model, as shown in Figure 2.

In the beginning of the calculation, the volume of the injected gas and the volume ratio of the components are set at the current calculation step. Then, the mass of the two-phase (slag–metal) system is set, and the units of all the components in the gas–slag–metal system are converted into the corresponding molar amounts. Next, the initial value of the iterative calculation is set and is used in Eqs. [5] through [9]. The solution is obtained through achieving the minimum value of the nonlinear multivariate function with the constraint conditions. In this method, a barrier function is introduced in the original objective function to replace the inequality constraint. These problems are easier to solve than the original quality-constrained problem.[40] When the tolerance is less than $1e^{-6}$ or the maximum number of iteration steps reaches 10,000, the iterative calculation result is the system component composition within the current time-step. After removing the gas phase components, the molar weight of the slag in the two-phase system of slag–metal is taken as the initial condition for the $t + 1^{th}$ calculation. The preceding steps are repeated until the injection cutoff time is reached.

The standard molar Gibbs free energy and standard states of the system components are listed in Table III.[41] The standard state of the gas phase is a pure substance, that of carbon and oxygen in the metal phase corresponds to 1 wt pct Henrian activity, and that of iron in the metal phase and ferrous oxide in the slag phase is a pure liquid substance.

The activity calculation formula for carbon and oxygen in the melt[42,43] is shown in Eqs. [16] and [17]. The standard state of iron in the melt is a pure liquid substance, and the activity is the mass fraction of iron. Iron oxides in the slag phase coexist as ferrous and ferric oxides. The mass ratio of ferrous oxide to ferric oxide[44] is 0.9251:0.0749, and the activity of ferrous oxide is 0.9293. The model is also applicable for analyzing the injection of O_2–CO_2–CO–inert gas (N_2/Ar) mixtures into the Fe–C melt.

$$\begin{aligned} aC &= wC, pct \times fC \\ &= wC, pct \times 10^{(158/T + 0.0581) \times wC, pct - 0.34 \times wO, pct} \end{aligned} \tag{16}$$

$$\begin{aligned} aO &= wO, pct \times fO \\ &= wO, pct \times 10^{-0.45 \times wC, pct + (0.734 - 1750/T) \times wO, pct} \end{aligned} \tag{17}$$

$$aFe = wFe, pct /100 \tag{18}$$

$$aFeO = 0.9293 \tag{19}$$

$$\begin{aligned} p_{CO_2} &= \frac{n_{CO_2}}{n_{CO_2} + n_{CO} + n_{O_2}} \\ p_{CO} &= \frac{n_{CO}}{n_{CO_2} + n_{CO} + n_{O_2}} \\ p_{O_2} &= \frac{n_{O_2}}{n_{CO_2} + n_{CO} + n_{O_2}} \end{aligned} \tag{20}$$

where $w_{i,pct}$ is the mass percentage of i; f_i is the Henrian activity coefficient of i; and T is the reaction temperature, K.

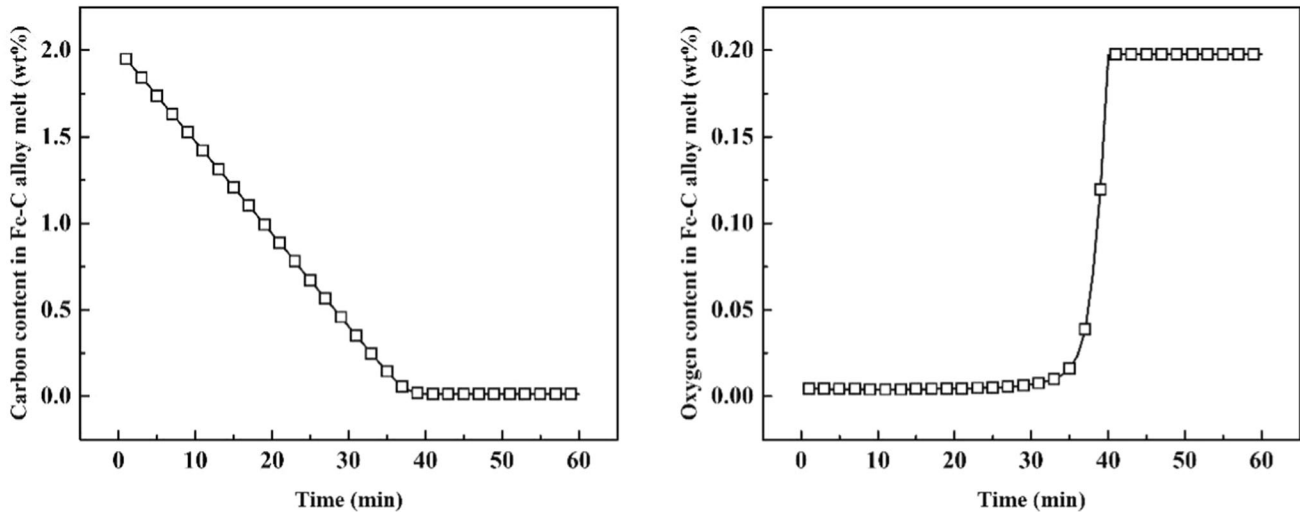| Temperature (K)	Metal Phase Mass (g)	Initial Carbon Content (Wt Pct)	Initial Oxygen Content (Wt Pct)	CO₂ Flow Rate (mL min⁻¹)	Time (min)
1873	1000	2	0.0012	1000	60

Fig. 3—Carbon and oxygen contents variation with time when blowing CO_2 into Fe–C melt with the initial carbon content of 2 wt pct.

III. CALCULATING RESULTS AND ANALYSIS

A. *Reaction Process of CO_2 Continuously Injected into the Fe–C Melt with Medium Carbon Content*

To study the reaction phenomenon or process between the injected CO_2 gas and Fe–C melt with medium carbon content, 2 wt pct was selected as the initial carbon content for the calculation. The injection time was 60 minutes, and the calculation step was 1 minute. The calculation boundary conditions are listed in Table IV.

Calculated with the model described in Section II, the variation of carbon and oxygen in the melt with time during blowing CO_2 into the Fe–C melt with the initial carbon content of 2 wt pct is shown in Figure 3. The change of gas volume and the variation of the volume ratio of CO_2 and CO in the gas phase with time are presented in Figures 4 and 5, respectively.

According to the calculation results shown in these figures, the reaction process can be divided into three stages. The first stage is from the beginning to the 34th minute, and the main feature is that the carbon content in the melt decreases continuously, whereas the oxygen content in the melt is maintained on the order of 10^{-3} wt pct. The second stage is from the 35th to the 40th minute; in this stage, the volume ratio of CO and the volume of the gas phase decrease rapidly, and the volume ratio of CO_2 increases. Meanwhile these results show that the oxygen content in the melt increases rapidly. The third stage in from the 41st minute, where
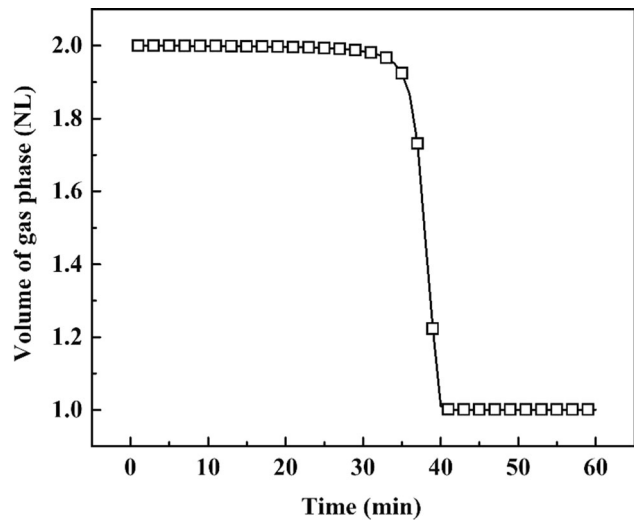

Fig. 4—Volume of gas phase variation with time when blowing CO_2 into Fe–C melt with the initial carbon content of 2 wt pct.

the system reaches the oxygen saturation state in the melt, which causes the volume and composition of the gas phase and the mass fraction of carbon and oxygen in the melt to remain unchanged. In this state, the gas phase volume is equal to the volume of CO_2 injected into the system; the volume ratios of CO and CO_2 are 85.75
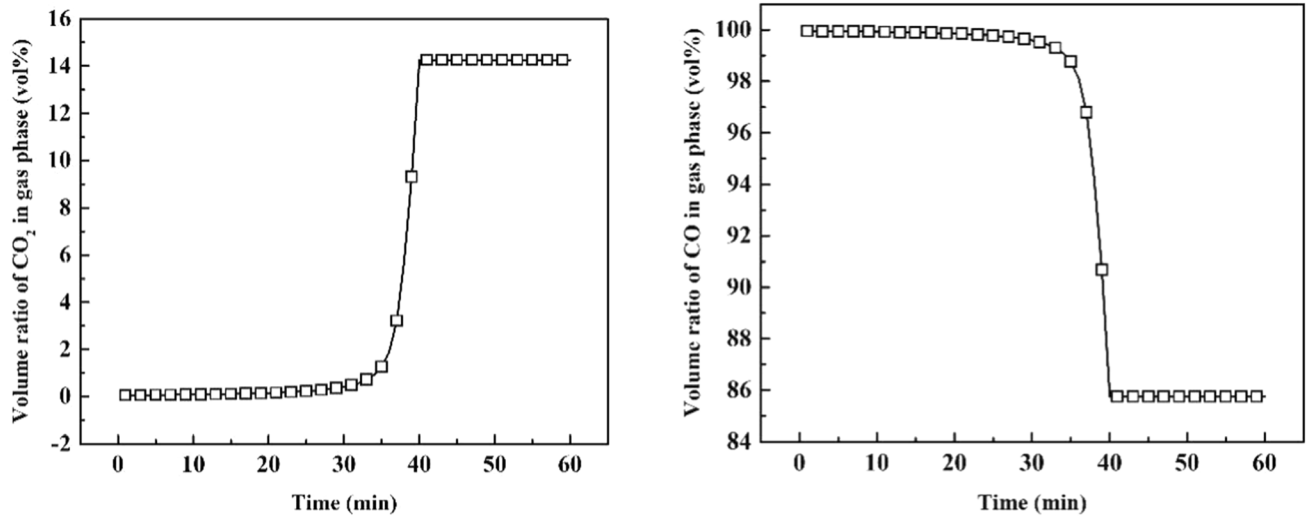
Fig. 5—Volume ratio of CO_2 and CO in gas phase variation with time when blowing CO_2 into Fe–C melt with initial carbon content of 2 wt pct.
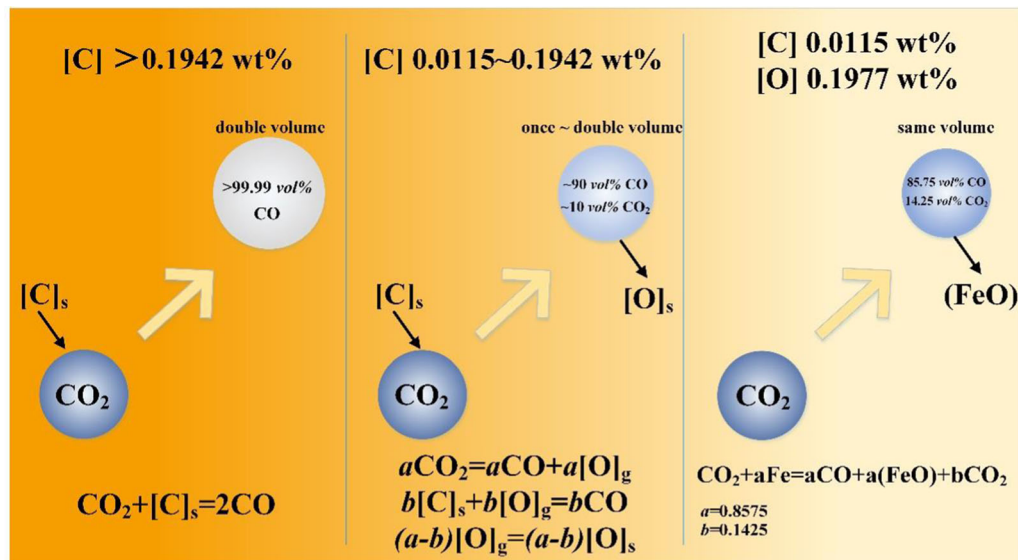

Fig. 6—Schematic of the reaction process between CO_2 and Fe–C melt with the initial carbon content of 2 wt pct.

and 14.25 vol pct, respectively; and the mass fractions of carbon and oxygen in the melt are 0.0115 and 0.1977 wt pct, respectively.

Figure 6 shows a schematic of the reaction process between the CO_2 gas and Fe–C melt when the initial carbon content is 2 wt pct under thermodynamic equilibrium. The reasons leading to the phenomena shown in Figures 3, 4 and 5 are discussed in the following sections. When CO_2 enters the melt, it firstly decomposes into CO and oxygen atoms. Under the condition of medium carbon content in the first stage, the oxygen content is extremely low (10^{-3} wt pct) when carbon and oxygen reach thermodynamic equilibrium with CO gas, and the oxygen content is almost unchangeable with time. Therefore, the oxygen atoms decomposed by CO_2 mainly react with carbon in the melt to form CO gas, which is twice as much as the injection volume. At this stage, the CO_2 gas facilitates the decarburization process and the overall reaction mechanism is $CO_2 + [C] = 2CO$. In the second stage, with the continuous injection of CO_2, the content of carbon in the melt decreases and the corresponding equilibrium oxygen concentration increases sharply (order of magnitude increases from 10^{-3} to 10^{-1} wt pct). Most of the oxygen atoms resulting from CO_2 decomposition participate in the decarburization reaction, and a part of oxygen atoms dissolves in the melt, leading to the decrease of gas volume in the system.

In the third stage, that is, when the system reaches the oxygen saturation state, the oxygen partial pressure (p_{O_2}) is usually used to characterize the oxidation ability of the phase. One can compare the p_{O_2} of the gas and metal phases to explain the final equilibrium state of the CO_2 injection process. The p_{O_2} of CO_2–CO mixtures with different CO and CO_2 proportions can be obtained by combining the isothermal equation of the chemical reaction (Eq. [22]), mass conservation equation (Eq. [23]), and calculation equation of partial pressure of the gas component (Eq. [24]). The p_{O_2} of the Fe–O_{sat}–C melt (w_O = 0.1977 wt pct) can be calculated as 4.75×10^{-9} atm with $0.5O_2$ = [O].

$$CO + 0.5O_2 = CO_2$$
$$\Delta G^{\Theta} = -278541.4 + 83.965T \text{ (J/mol)} \quad [21]$$
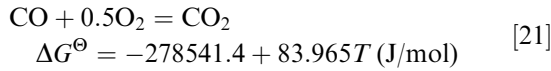
$$\Delta G^{\Theta} = -RT \ln \frac{p_{CO_2}^*}{p_{CO}^* \times (p_{O_2}^*)^{0.5}} \quad [22]$$

$$
\begin{aligned}
n_{CO_2}^* &= n_{CO_2}^0 - n^{\text{rect.}} \\
n_{CO}^* &= n_{CO}^0 + n^{\text{rect.}} \\
n_{CO}^* &= n_{O_2}^0 + 0.5 \times n^{\text{rect.}}
\end{aligned}
\quad [23]
$$

$$
\begin{aligned}
p_{CO_2}^* &= \frac{n_{CO_2}^*}{n_{CO_2}^* + n_{CO}^* + n_{O_2}^*} \\
p_{CO}^* &= \frac{n_{CO}^*}{n_{CO_2}^* + n_{CO}^* + n_{O_2}^*} \\
p_{O_2}^* &= \frac{n_{O_2}^*}{n_{CO_2}^* + n_{CO}^* + n_{O_2}^*}
\end{aligned}
\quad [24]
$$

where n_i^* and p_i^* are the molar mass and partial pressure of i in thermodynamic equilibrium, respectively (mol/atm).

From Figure 7, it is seen that when the proportion of CO_2 increases in the CO_2–CO mixture, the corresponding p_{O_2} also increases and the p_{O_2} corresponding to the pure CO_2 gas is 0.00348, which is much higher than that corresponding to oxygen saturation in the Fe–C melt (horizontal dash line in Figure 7). Therefore, in the third stage, as the reaction progresses, the pure CO_2 gas continuously transfers oxygen atoms to the Fe–C melt, which will react with iron and exist as iron oxide in the system. When the proportion of CO_2 in the CO_2–CO mixture is 14.25 vol pct, the mixed gas is injected into the Fe–C melt with saturated oxygen content, the mixed gas no longer transfers oxygen to the melt, and the composition of each component in the system does not change. From the preceding analysis, we can infer that when the CO_2–CO mixture is continuously injected into the Fe–C–O melt and when the proportion of CO_2 in the gas mixture is more than 14.25 vol pct, the gas phase volume is equal to the volume of the CO_2–CO mixture
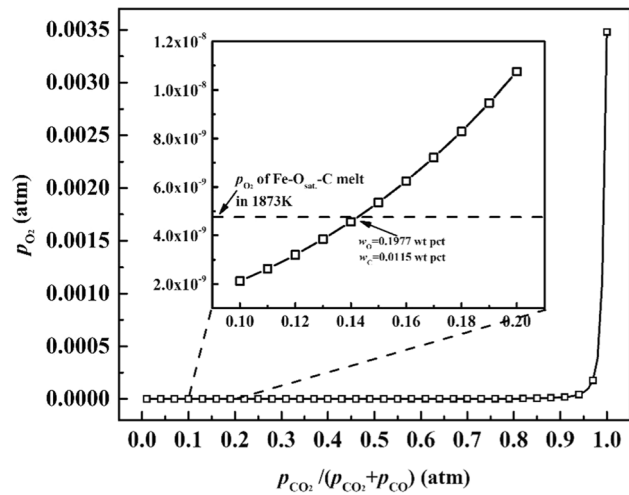

Fig. 7—Relationship between the volume ratio of CO_2 in the CO–CO_2 mixture and p_{O_2}.

injected into the system under the equilibrium state. The volume ratio of CO in the gas phase is 85.75 vol pct, and that of CO_2 maintains at 14.25 vol pct; the mass fractions of carbon and oxygen in the melt are 0.0115 and 0.1977 wt pct, respectively. When the proportion of CO_2 in the CO_2–CO mixture is less than 14.25 vol pct, the oxygen partial pressure corresponding to the melt is equal to the oxygen partial pressure corresponding to the CO_2–CO mixture and the oxygen concentration in the melt will be lower than 0.1977 wt pct.

The preceding discussion shows that, when the carbon content in the metal phase is 0.05 wt pct, the volume of the gas phase is 1.67 times that of the initial injection gas volume during the CO_2 gas continuously being injected into the melt and the volume of CO gas in the gas phase is 96.14 pct. During industrial production, the carbon content at the end of the smelting process is around 0.04 to 0.06 wt pct in the BOF and EAF. Therefore, it is appropriate to use CO_2 gas as the bottom-blowing medium in the BOF and EAF because CO_2 can react with the carbon in the melt to generate twice the volume of CO gas in most smelting processes, which can effectively enhance the stirring intensity of the molten pool.

B. Reaction Process of CO_2 Continuously Injected into the Fe–C Melt with Extremely Low Carbon Content

The reaction process for CO_2 gas injected into the Fe–C melt with extremely low carbon content was examined to fully understand the CO_2 effect in the entire decarburization process, especially the change of components in the system. In this case, pure iron melt under ideal conditions was selected as the metal phase. The injection time was 60 minutes, and the calculation step was set as 1 minute. The boundary conditions used for the calculations are given in Table V, while the calculated results are shown in Figures 8 through 10.

Table V. Boundary Conditions Used for Calculations during CO_2 Injection into Fe–C Melt With Extremely Low Carbon Content

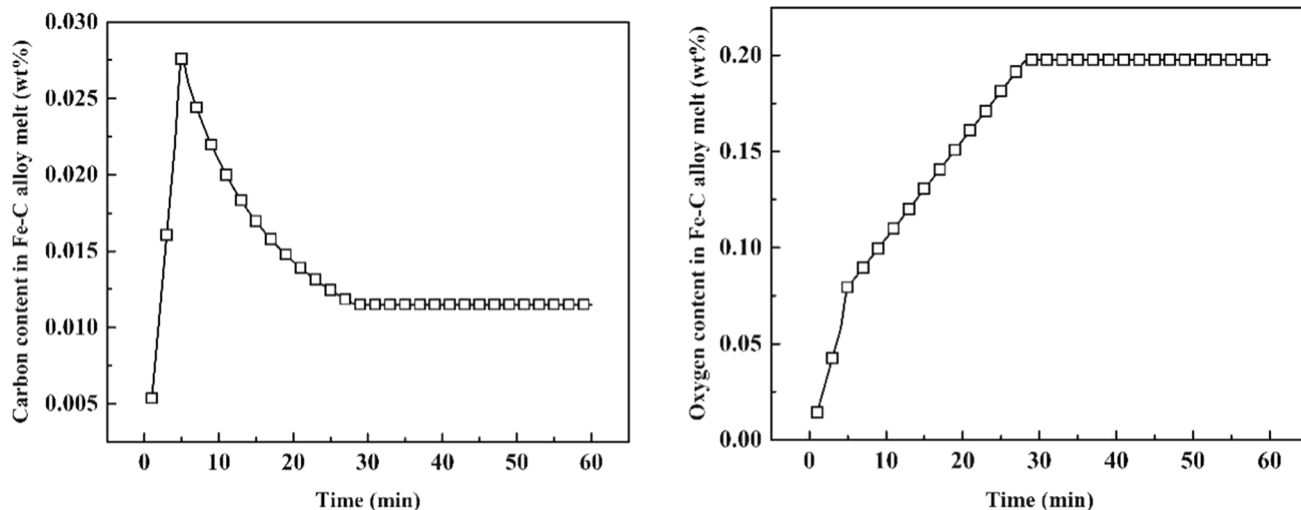| Temperature (K)	Metal Phase (mass/g)	Initial Carbon Content (Wt Pct)	Initial Oxygen Content (Wt Pct)	CO_2 Flow Rate (mL min^{-1})	Time (min)
1873	1000	0	0	100	60

Fig. 8—Variation of carbon and oxygen contents with time in the melt of pure iron.
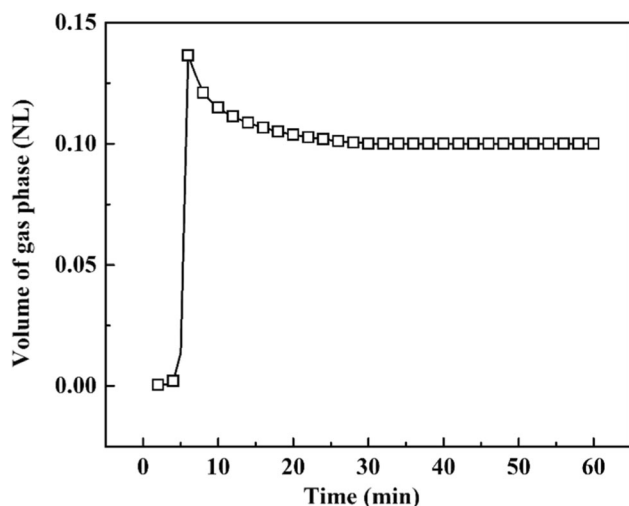
Fig. 9—Variation of gas phase volume with time in the melt of pure iron.

As seen from Figures 8 through 10, the reaction process for CO_2 injecting into the Fe–C melt with pure iron can be divided into three stages. The first stage is from the beginning to the 4th minute, which is characterized by the complete decomposition of CO_2 in the melt, generating carbon and oxygen; in this case, the mass fractions of carbon and oxygen in the metal phase increase rapidly. The second stage is from the 5th to 28th minute. In the 5th minute, the gas phase volume is nearly twice and the carbon content in the melt reaches its maximum value. After the 5th minute, the volume of the gas phase and the volume fraction of CO in the gas phase gradually decrease, while the volume fraction of CO_2 increases. Meanwhile, the carbon content decreases and the oxygen content continuously increases. From the 29th minute, the system reaches the oxygen saturation state in the melt, which is taken as the third stage.

Figure 11 shows the reaction mechanism or process of CO_2 gas injected into the Fe–C melt when the initial metal phase is pure iron. The reasons leading to the phenomena shown in Figures 8 through 10 are explained subsequently. When CO_2 enters the Fe–C melt, it first decomposes into CO and oxygen atoms and the $a_{[O]} \times a_{[C]}$ values in the pure iron melt are still considerably lower than those obtained in equilibrium with CO gas; thus, CO gas cannot be produced. Therefore, the overall reaction mechanism of CO_2 gas reacting with elements in the melt can be represented as $CO_2 = [C] + 2[O]$. In this case, the role of CO_2 gas is to increase the amounts of oxygen and carbon. This situation is usually seen in the refining process. After the decarburization reaction in the primary refining furnace (BOF or EAF), the carbon content of molten steel at the end of smelting is relatively low. At the same time, owing to deoxidization and alloying during tapping, the dissolved oxygen content in the molten steel is extremely low. Therefore, if CO_2 gas is injected into the molten steel during the refining process (LF, VD, or RH), it will be partially or completely dissolved in molten steel, thus adding oxygen and carbon to the molten steel, which reduces the effect
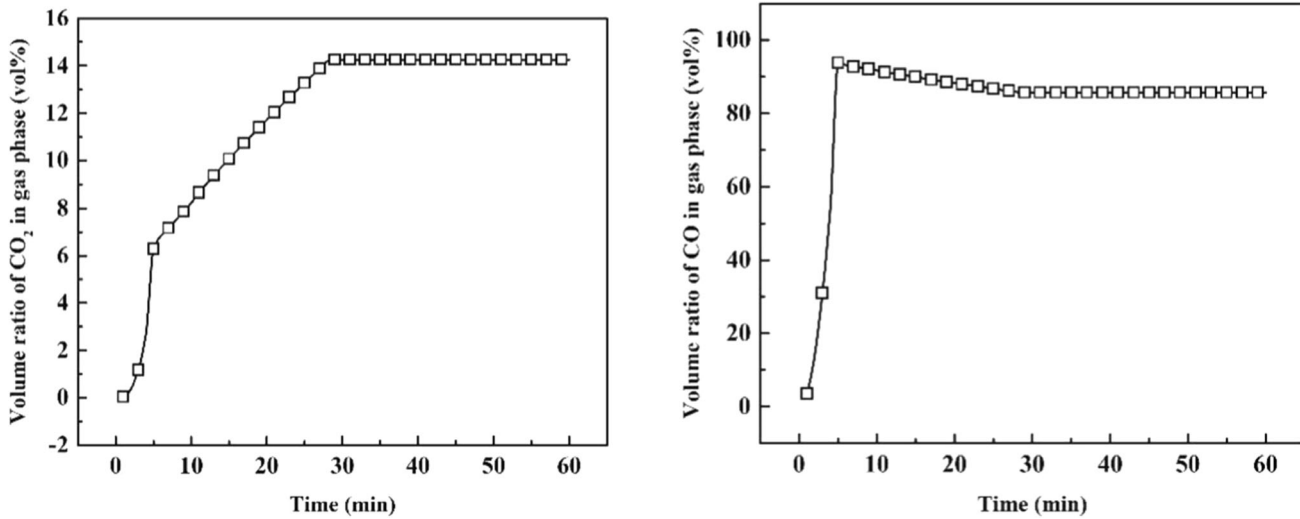
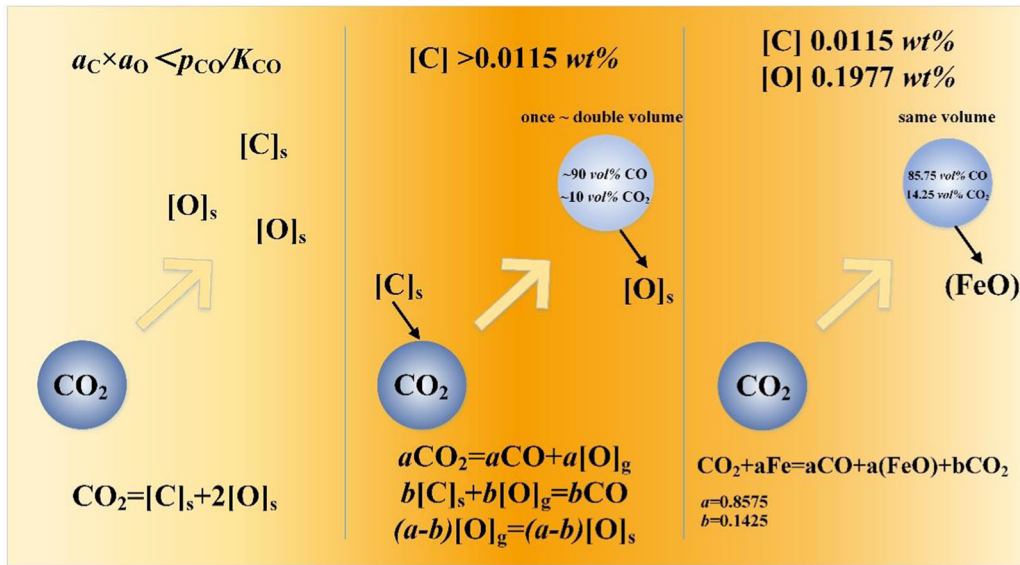Fig. 10—Variation of volume ratio of CO_2 and CO in gas phase with time in the melt of pure iron.

Fig. 11—Reaction mechanism of CO_2 gas reacting with the melt of pure iron.

of bottom blowing. Hence, using CO_2 instead of Ar may not be suitable for the refining process, which needs to be verified by experiments.

With the rapid increase of carbon and oxygen content in the melt, $a_{[O]} \times a_{[C]}$ can be balanced with CO in the gas phase after 5 minutes. However, the oxygen partial pressure corresponding to the oxygen in the melt is still considerably lower than that corresponding to CO_2 gas. Therefore, as the reaction progresses, CO_2 gas continuously transfers oxygen atoms to molten steel. In this process, due to the continuous increase of oxygen content in molten steel, in order to maintain the reaction equilibrium between carbon and oxygen with CO gas, the carbon content will decrease accordingly. When the reaction lasted for 29 minutes, the oxygen content in the melt reached a saturation state.

IV. EXPERIMENTS AND DISCUSSION

To verify the accuracy of the model, experiments involving the injection of CO_2 gas into the Fe–C melt with different initial carbon contents were carried out. In part of theoretical calculation, the Fe–C melt with 2 wt pct carbon content was selected to analyze the effect of CO_2 on the reaction process. In this system, the CO_2 gas mainly plays the role of decarburization for the medium carbon melt, which has been proved by previous research. Therefore, we chose the carbon content of 0.01 to 0.05 wt pct in the experimental scheme to mainly verify the carbon content in the equilibrium state when CO_2 was continuously injected into the Fe–C alloy melt with low carbon content. In addition, there is no pure iron (the content of carbon and oxygen is 0), so two very

Table VI. Experimental Parameters

Item	Mass (g)	Initial Carbon Content (Wt Pct)	Temperature (K)	CO_2 Flow Rate (mL·min^{-1})	Injection Intensity (mL·min^{-1}·g^{-1})
1	600	0.048	1873	100	0.1667
2	600	0.039	1873	100	0.1667
3	600	0.029	1873	100	0.1667
4	600	0.01	1873	100	0.1667
5	600	0.0056	1873	100	0.1667
6	600	0.0042	1873	100	0.1667

Table VII. Chemical Composition of Electrolytic Iron

Elements	C	Si	Mn	P	S	O
ppm	4	< 5	4	3	4	60

low carbon contents of 0.004 and 0.006 wt pct were selected as experimental conditions to verify the recarburization behavior of CO_2 gas in the Fe–C melt with extremely low carbon content. The experimental parameters are given in Table VI.

A. Experimental Apparatus and Process

The Fe–C alloy was prepared from electrolytic iron (1-s grade, produced by Toho Zinc Co., Ltd., Tokyo) and graphite powder (chemical pure, produced by Sinopharm Chemical Reagent Co., Ltd.). The composition of the industrial pure iron is given in Table VII.

The Fe–C alloy was prepared as follows.

(1) 600 g of electrolytic iron and graphite powder were weighed for preparing the alloy. The prepared Fe–C mixture was placed in an Al_2O_3 crucible with an outer diameter of 70 mm, an inner diameter of 50 mm, and a height of 195 mm. The crucible was placed in the constant-temperature zone of the tubular furnace. The experimental setup is shown in Figure 12.
(2) High-purity argon was introduced into the corundum furnace tube from the bottom of the tube furnace and the temperature increased after 5 minutes of emptying.
(3) During the heating and melting processes, the flow rate of argon at the bottom was maintained at 200 mL·min^{-1}. After the temperature of the tubular furnace reached the reaction temperature, the temperature was maintained for 30 minutes so that the Fe and C elements were evenly mixed and the Fe–C alloy was formed.

CO_2 injection into the Fe–C melt was performed as follows.

(1) After the Fe–C alloy was prepared, the melt sample was extracted using the sampler as the initial sample.
(2) A 6-mm corundum tube was used to connect the CO_2 gas supply system, and the corundum tube was
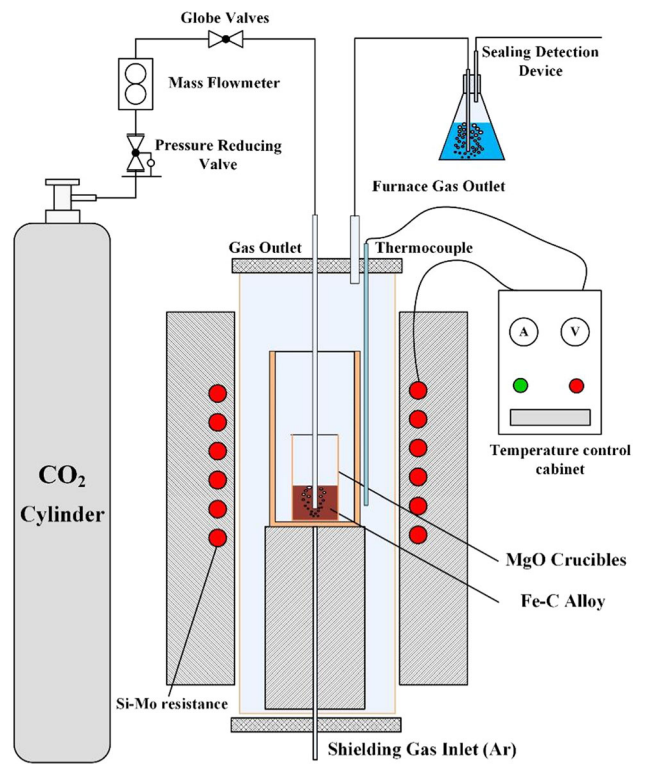

Fig. 12—Schematic of the experimental apparatus.

inserted into the bottom of the molten steel to blow CO_2 for 5 minutes. After blowing for 5 minutes, the sample was collected with a quartz tube.
(3) The sampling method was as follows: First, the quartz tube was inserted into the Fe–C melt (about 1 cm away from the bottom of the crucible); then, a pipette was used to extract a 6-mm-diameter rod with a length of approximately 5 to 8 cm.

The carbon content was determined using a carbon sulfur analyzer (EMIA-820V, Horiba, Kyoto), and the oxygen content in the sample was determined using an ONH instrument (TCH-600, LECO*).

---

*LECO is a trademark of LECO Corporation, St. Joseph, MI.

B. *Experimental Results and Discussion*

The changes of carbon content with time during CO_2 injection into the Fe–C melt with different initial carbon contents were analyzed, and the results are shown in Figure 13. As seen in the figure, when the initial carbon content was greater than 0.01 wt pct, the carbon content decreased with the continuous blowing of CO_2 gas into the melt and finally stabilized at approximately 0.011 wt pct. When the initial carbon content was 0.01 wt pct, the carbon content in the melt fluctuated from 0.01 to 0.011 wt pct after CO_2 injection. This experimental result agrees with the theoretically calculated carbon content of the metal under final equilibrium state after injecting CO_2 into the Fe–C melt with medium carbon content.

When the initial carbon contents were 0.004 and 0.006 wt pct, the carbon content increased linearly with time and finally stabilized to 0.011 wt pct. The calculation results prove that CO_2 gas injection increases the carbon content into the Fe–C melt when the initial carbon content is lower than the final equilibrium carbon content.

To further study the variation of the melt composition when CO_2 gas is injected into the Fe–C melt with an extremely low carbon content and determine the maximum carbon content in molten steel during theoretical calculations, another group of experiments was carried out. In these experiments, the injection intensity was reduced, that is to say, the liquid mass was increased, and the CO_2 injection flow rate was reduced. The liquid mass was set at 1000 g, and the CO_2 gas injection flow rate was set at 50 mL min^{-1}. When the injection intensity was 0.05 mL min^{-1} g^{-1}, the initial carbon and oxygen contents in the Fe–C melt were 0.0072 and 0.0270 wt pct, respectively. Argon is introduced into the bottom of the tubular furnace as a shielding gas, and the flow rate is 950 mL·min^{-1}.

The variations of the carbon and oxygen contents in the melt with time are shown in Figures 14 and 15, respectively. It is seen from Figure 14 that the carbon content increases with time during the experiments and reaches the extreme peak in the 15th minute; then, it decreases to the final equilibrium value (0.011 wt pct). However, the peak value is less than the results obtained from the theoretical calculation, and the time to reach the maximum value is later than that of the theoretical calculation, which may be because the oxygen is the
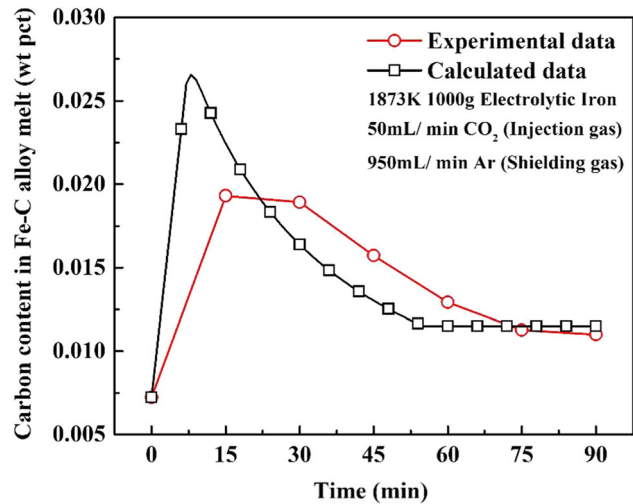

Fig. 14—Carbon content variation with time when the injection gas is CO_2.
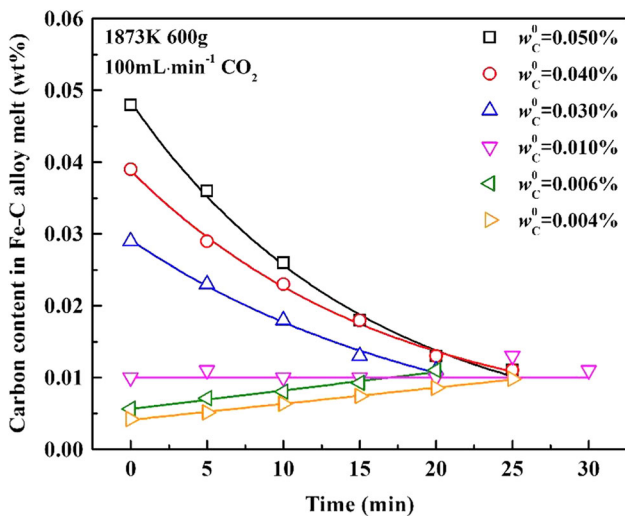

Fig. 13—Carbon content variation with time when the initial carbon content is less than 0.05 wt pct.
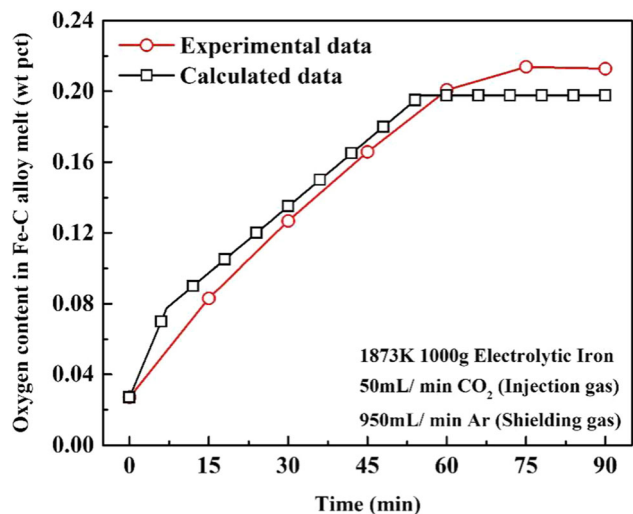

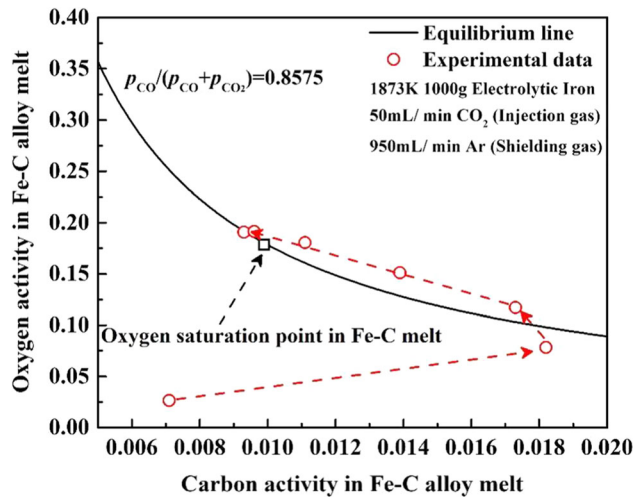Fig. 15—Oxygen content variation with time when the injection gas is CO_2.

Fig. 16—Comparison of the final equilibrium state and the experimental activity changes of carbon and oxygen with CO_2 continuously injecting into the Fe–C melt.

main surface-active element in the iron-based melt. The high oxygen concentration in the melt hinders the decomposition reactions of CO_2 and CO in the Fe–C melt with an extremely low carbon content, resulting in the gas not reaching the thermodynamic equilibrium state during the bubble rising process of the molten pool. The kinetics of the process requires further study. Meanwhile, the oxygen content in the melt increased with time and reached the saturation concentration (0.2127 wt pct) in 75 minutes, which was slightly higher than the theoretical calculation results, as can be seen in Figure 15.

In order to more intuitively observe the change of carbon and oxygen activity when CO_2 gas was continuously injected into the Fe–C melt under the condition of extremely low carbon content, Figure 16 is drawn and the change track with time (0 to 90 minutes) follows the red arrow in the figure. As seen in the figure, at 0 and 15 minutes, the carbon and oxygen activity products are all lower than the equilibrium line. After 30 minutes, the carbon and oxygen activity product of liquid steel is higher than the equilibrium line. Then, the carbon activity decreases and the carbon and oxygen activity product moves to the oxygen saturation point. Therefore, it can be concluded that, when CO_2 gas is continuously injected into the Fe–C melt, whose initial carbon and oxygen activity point is above the equilibrium line, the carbon in the melt can be removed by CO_2 gas, while, if the initial activity point of carbon and oxygen is below the equilibrium line, CO_2 gas increases carbon and oxygen content into the melt. Finally, the Fe–C melt reaches the equilibrium point, that is, the oxygen element is saturated in the Fe–C melt.

V. CONCLUSIONS

Based on the thermodynamic calculation and experiments in the laboratory, the final reaction equilibrium state and process were studied by injecting CO_2 into the Fe–C melt under different initial carbon contents. The following conclusions were obtained.[n12]

1. At 1873 K, the oxygen partial pressure corresponding to CO_2 gas is 0.0035 atm, which is much higher than that corresponding to the oxygen saturation in the Fe–C melt. Therefore, when CO_2 is continuously injected into the Fe–C melt, the final equilibrium state of the system is such that the oxygen content reaches saturation (0.1977 wt pct) and the carbon content is 0.0115 wt pct. In the final equilibrium state, 85.75 vol pct of the injected CO_2 gas is decomposed into CO gas and oxygen atoms, and the oxygen and iron atoms react to form iron oxide in the system.

2. It is generally believed that CO_2 plays a role in decarburization when it reacts with the Fe–C alloy. However, when the initial $a_{[O]} \times a_{[C]}$ in the melt is less than those in equilibrium with 0.8575 atm CO in 1873 K, the role of CO_2 gas is to add carbon and oxygen to the melt until the system reaches equilibrium. Further injection of CO_2 gas may lead to oxygen saturation in the melt.

3. By comparing the theoretical calculation with the experimental data, it is verified that the final equilibrium state is carbon content 0.011 wt pct and oxygen concentration 0.2 wt pct when CO_2 is continuously injected into the Fe–C melt at 1873 K. When the initial carbon and oxygen contents were 0.0072 and 0.0270 wt pct, the peak value of carbon content was less than the theoretical value and the time to reach the peak was behind the theoretical calculation in the process of continuously injecting CO_2 into Fe–C melt. The reason for this requires further study.

4. The industrial test results of the 300t converter bottom blowing different gas media show that the end carbon and oxygen product of the entire process of bottom blowing CO_2 is higher than that of the entire process of bottom blowing inert gas. The end carbon and oxygen product of the bottom blowing CO_2–Ar is 15.33×10^{-4}, similar to the bottom blowing inert gas in the entire process.

CONFLICT OF INTEREST

On behalf of all authors, the corresponding author states that there is no conflict of interest.

OPEN ACCESS

REFERENCES

1. C. Yi, R. Zhu, B.Y. Chen, C.R. Wang, and J.X. Ke: *ISIJ Int.*, 2009, vol. 49, pp. 1694–99.
2. M. Lv, R. Zhu, X. Wei, H. Wang, and X. Bi: *Steel Res. Int.*, 2012, vol. 83, pp. 11–15.
3. P. Blostein, D. Gortan, and K. Stephens: in *73rd Steelmaking Conf. Proc.*, Detroit, 1990, pp. 315–18.
4. X.L. Wang, R. Zhu, B.L. Zhang, J.M. Bian, Y.Q. Zhu, and W.H. Wu: in *2017 Mater. Sci. Technol. Conf.*, Chengdu, 2017, pp. 712–18.
5. M. Lv, R. Zhu, and L. Yang: *Steel Res. Int.*, 2019, vol. 90, p. 1800454.
6. W. Du, Y. Wang, and X.P. Liang: *JOM.*, 2017, vol. 69, pp. 1785–89.
7. W.T. Du, Q. Jiang, Z. Chen, X.P. Liang, and Y. Wang: *JOM.*, 2019, vol. 71, pp. 4925–30.
8. G. Wei, R. Zhu, K. Dong, Z. Li, L. Yang, and X. Wu: *Ironmak. Steelmak.*, 2018, vol. 45, pp. 839–46.
9. T. Bruce, F. Weisang, M. Allibert, and R. Fruehan: in *7th Proc*, Electric Furnace Conf, Chicago, IL, 1987, pp. 293–97.
10. Y. Gu, H. Wang, R. Zhu, J. Wang, M. Lv, and H. Wang: *Steel Res. Int.*, 2014, vol. 85, pp. 589–98.
11. B. Han, R. Zhu, Y. Zhu, R. Liu, W. Wu, Q. Li, and G. Wei: *Metall. Mater. Trans. B.*, 2018, vol. 49B, pp. 3544–51.
12. B. Han, R. Zhu, C. Feng, W. Li, G. Wei, Z. Wang, and Q. Li: *Vacuum*, 2020, vol. 179, p. 109520.
13. B. Han, R. Zhu, G. Wei, C. Feng, and J. Dong: in *Energy Technology 2020*. Cham, 2020, vol. 2020, pp. 99–110.
14. R. Wang, Z. Yuan, S. Xie, J. Li, N. Hai, and J. Zhai: *J. Iron Steel Res.*, 2018, vol. 30, pp. 874–80. (in Chinese).
15. P.A. Distin: Ph.D. Thesis, University of London, London, 1967.
16. Y. Niiri, K. Ito, and K. Sano: *Tetsu-to-Hagané.*, 1969, vol. 55, pp. 437–45.
17. S. Anezaki, K. Shimizu, and T. Mori: *Tetsu-to-Hagané*, 1971, vol. 57, pp. 1109–22.
18. H. Nomura and K. Mori: *Tetsu-to-Hagané*, 1972, vol. 58, pp. 1603–11.
19. H. Nomura, K. Mori, and Y. Shirota: *Tetsu-to-Hagané*, 1974, vol. 60, pp. 361–71.
20. R.J. Fruehan and L.J. Martonik: *Metall. Trans.*, 1974, vol. 5, pp. 1027–32.
21. N.H. El-kaddah and D.G.C. Robertson: *Metall. Trans. B.*, 1978, vol. 9B, pp. 191–99.
22. H.G. Lee and Y.K. Rao: *Metall. Trans. B.*, 1982, vol. 13B, pp. 403–09.
23. H.G. Lee and Y.K. Rao: *Metall. Trans. B.*, 1982, vol. 13B, pp. 411–21.
24. F.J. Mannion and R.J. Fruehan: *Metall. Mater. Trans. B.*, 1989, vol. 20B, pp. 853–61.
25. T. Nagasaka and R.J. Fruehan: *ISIJ Int.*, 1994, vol. 34, pp. 241–46.
26. N. Simento, H.G. Lee, and P. Hayes: *Steel Res. Int.*, 1998, vol. 69, pp. 318–24.
27. N.J. Simento, H.-G. Lee, and P.C. Hayes: *ISIJ Int.*, 1999, vol. 39, pp. 1217–23.
28. H. Ono-Nakazato, Y. Morita, K. Tamura, T. Usui, and K. Marukawa: *ISIJ Int.*, 2001, vol. 41, pp. S61–65.
29. K. Taguchi, H. Ono-Nakazato, T. Usui, and K. Marukawa: *Metall. Mater. Trans. B.*, 2003, vol. 34B, pp. 861–67.
30. H.D. Zughbi: *Scand. J. Metall.*, 2003, vol. 32, pp. 194–202.
31. H.D. Zughbi: *Scand. J. Metall.*, 2004, vol. 33, pp. 242–50.
32. S.H. Jung: *Master's Thesis*, Pohang University of Science and Technology, Pohang, 2010, pp. 68–70.
33. H. Wang: Ph.D. Thesis, Royal Institute of Technology, Stockholm, 2010, pp. 5–36.
34. C.P.P. Wu: Ph.D. Thesis, University of Toronto, Toronto, 2015.
35. Y. Fan, X. Hu, R. Zhu, and K. Chou: *ISIJ Int.*, 2020, vol. 60, pp. 848–55.
36. Y. Fan, X. Hu, R. Zhu, and K. Chou: *Steel Res. Int.*, 2020, vol. 91, p. 2000127.
37. I.-H. Jung, S.A. Decterov, and A.D. Pelton: *Metall. Mater. Trans. B.*, 2004, vol. 35B, pp. 493–507.
38. R. Sarkar, P. Gupta, S. Basu, and N.B. Ballal: *Metall. Mater. Trans. B.*, 2015, vol. 46B, pp. 961–76.
39. A. Kruskopf and V.-V. Visuri: *Metall. Mater. Trans. B.*, 2017, vol. 48B, pp. 3281–300.
40. R.H. Byrd, M.E. Hribar, and J. Nocedal: *SIAM J. Optim.*, 1999, vol. 9, pp. 877–900.
41. X.H. Huang: *Principles of Ironmaking and Steelmaking*, Metallurgical Industry Press, Beijing, 2013, p. 631.
42. Y. Lytvynyuk: Ph.D. Thesis, Montan University of Leoben, Leoben, 2013, p. 40.
43. G.K. Sigworth and J.F. Elliott: *Met. Sci.*, 1974, vol. 8, pp. 298–310.
44. C.W. Bale, E. Bélisle, P. Chartrand, S.A. Decterov, G. Eriksson, A.E. Gheribi, K. Hack, I.H. Jung, Y.B. Kang, J. Melançon, A.D. Pelton, S. Petersen, C. Robelin. J. Sangster, P. Spencer, and M.-A. Van Ende: FactSage Thermochemical Software and Databases—2010–2016. *Calphad*, 2016, vol. 54, pp. 35–53, http://www.factsage.com.